Open Access
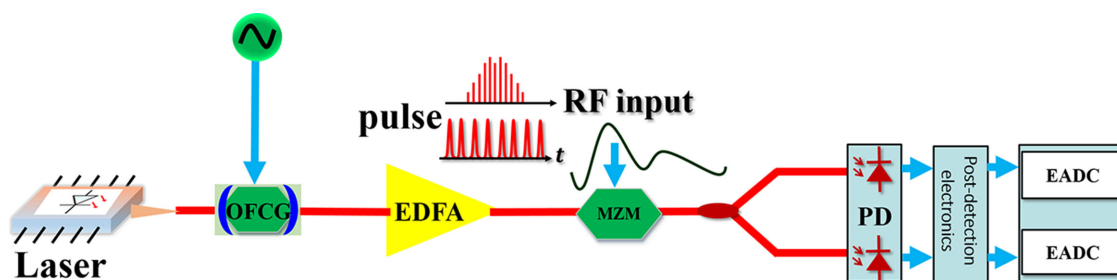
Broadband Photonic Down-Conversion Preprocessor for ADC With Arcsine Equalization

Rui Guo
Yankun Li
Chenbo Zhang
Peng Lei
Qing Yin
Xiaopeng Xie
Zhangyuan Chen

Broadband Photonic Down-Conversion Preprocessor for ADC With Arcsine Equalization

Rui Guo [ID],[1] **Yankun Li,**[1] **Chenbo Zhang,**[1] **Peng Lei** [ID],[1] **Qing Yin** [ID],[1] **Xiaopeng Xie** [ID],[1] **and Zhangyuan Chen** [ID] [1,2,3]

[1]State Key Laboratory of Advanced Optical Communication Systems and Networks, Department of Electronics, Peking University, Beijing 100871, China
[2]Nano-optoelectronics Frontier Center of the Ministry of Education, Beijing 100190, China
[3]Peking University Shenzhen Institution, Shenzhen 518055, China

Abstract: It is a challenge to convert broadband millimeter-wave signals directly with electronic analog-to-digital converters (ADCs). The photonic down-conversion preprocessor is a promising solution. The arcsine equalization originated from the photonic sampled ADC is applied in the photonic down-conversion preprocessor to leverage the performance. We derive the working principle of the photonic down-conversion system with the arcsine equalization for the first time, and comprehensively investigate the evolution of signal-to-noise ratio (SNR) and signal-to-noise and distortion ratio (SINAD) after the equalization. It shows that the equalization works quite differently in the proposed system, effectively suppressing the nonlinearity from large modulation depth within a periodic frequency range. The common-mode noise is canceled and additional gain of SNR is achieved for any frequency. Factors affecting the performance are discussed in detail, guiding the optimal configuration to exploit the potential of the proposed system under different scenarios. Signals ranging from 31 GHz to 48.9 GHz are digitized via the proposed system with a bandwidth of 10 GHz and an effective number of bits (ENOB) of 5.9. A newly-defined figure of merit (FOM) is proposed to comprehensively and flexibly evaluate bandpass sampling systems and the proposed system displays a favourable performance.

Index Terms: Photonic preprocessor, digital signal processing, optical frequency combs.

1. Introduction

The fast development of communication, radar, and sensing results in an increased demand for the high-speed ADC with an uncompromised resolution [1]–[3]. However, the analog bandwidth of an electronic ADC is usually not large enough to directly process microwave and millimeter-wave signals. Optical frequency comb (OFC) can serve as a photonic preprocessor, down-converting microwave and millimeter-wave signals to the baseband without a local oscillator of certain frequency and enable detection with supporting circuits of low bandwidth before the electronic ADC [4]–[7]. Moreover, the frequency down-conversion with an OFC of low phase noise can reduce the
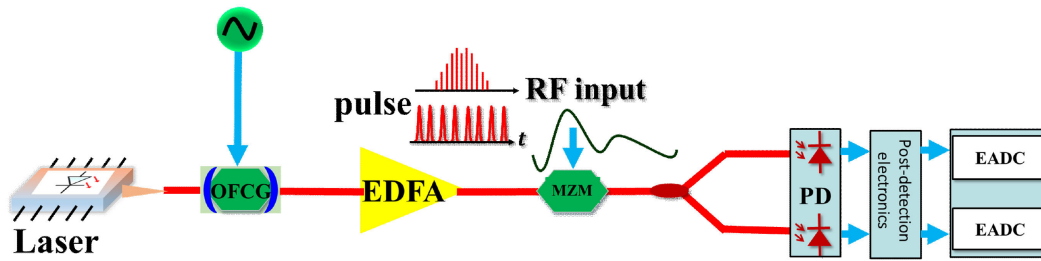
Fig. 1. The schematic diagram of the proposed photonic down-conversion preprocessor based on DO-MZM. OFCG: optical frequency comb generator; EDFA: erbium-doped fiber amplifier; MZM: dual output Mach-Zehnder modulator; RF: radio frequency; PD: photo-detector; and EADC: electronic ADC.

timing requirement of the electronic ADC because the impairment of precision from the electronic timing jitter is determined by the product of the electronic timing jitter and signal frequency into the electronic ADC [8]. Besides, the photonic down-conversion preprocessor allows the signal detection hardware to be remote from the antenna thanks to the low loss of optical fiber [9].

On the other hand, optical devices may introduce extra noise and distortion to the photonic down-conversion preprocessor. For example, the modulation nonlinearity may deteriorate the spurious-free dynamic range (SFDR) when one improves the SNR by increasing the modulation depth. This conflict needs to be resolved to realize the optimal performance of a photonic preprocessor. In the photonic sampled ADC with a similar structure, where the optical pulse works as the sampling gate [10]–[14], a simple but effective arcsine equalization based on a dual output Mach-Zehnder modulator (DO-MZM) was applied to ease the conflict [12], [14]–[15]. However, no detailed analysis has been proposed so far for the application of this arcsine method in the photonic down-conversion system. We will show theoretically and experimentally that the equalization works effectively but quite differently in the proposed photonic preprocessor due to no temporal pulse shape preserved before the electronic ADC. It is necessary and meaningful to explore the evolution of the SNR and SINAD with this nonlinear equalization in the photonic down-conversion system, seek for unique features and exploit these features to reach the potential of the system.

In this paper, we comprehensively derive the working principle of the photonic down-conversion preprocessor with the arcsine equalization and show a different feature of the equalization when applied in this system. The equalization cancels common-mode noise and maximally achieves 3-dB additional gain of SNR. The nonlinearity from large modulation depth is effectively suppressed within a periodic frequency range. The performance of the photonic down-conversion system with the arcsine equalization is theoretically analyzed and experimentally verified, providing guidance on the optimal configuration under different scenarios. Millimeter-wave signals from 31 GHz to 48.9 GHz are digitized through the proposed system with a large bandwidth of 10 GHz and ENOB of 5.9 (42.8 GHz) thanks to the analysis of optimization in this work. A new figure of merit for a comprehensive and flexible evaluation of bandpass sampling systems is proposed and our system is compared with the previous reports.

2. Operation Principle

2.1. Photonic Down-Conversion Preprocessor Based on DO-MZM

The schematic diagram of the proposed down-conversion photonic preprocessor based on DO-MZM is shown in Fig. 1. The electric field of the OFC can be expressed as

$$E_{in}(t) = A(t)e^{-j\omega_c t} \sum_{k=-\infty}^{+\infty} f(t - kT_0) = A(t)e^{-j\omega_c t} \sum_{k=-\infty}^{+\infty} a_k e^{-jk\omega_0 t} \tag{1}$$

in which

$$a_k = \frac{1}{T_0} FT[f(t)]_{\omega = \frac{2\pi k}{T_0}} \tag{2}$$

$f(t)$ represents the shape of the pulse within one period T_0. $\omega_0 = 2\pi/T_0$. ω_c is the angular frequency of the seed laser. $A(t)$ is the amplitude the electric field including the amplitude fluctuations resulting from the relative intensity noise (RIN) and amplified spontaneous emission (ASE) noise. $A(t)$ is normalized to 1 for an ideal pulse train. After the input radio-frequency (RF) signal modulating the OFC, the electric fields from the two output arms of DO-MZM working at the quadrature point are

$$E_{o1}(t) = \frac{A(t)}{2} e^{-j\omega_c t}(1 + e^{j\varphi(t) + j\pi/2}) \sum_{k=-\infty}^{+\infty} f(t - kT_0) \tag{3}$$

$$E_{o2}(t) = \frac{A(t)}{2} e^{-j\omega_c t}(1 - e^{j\varphi(t) + j\pi/2}) \sum_{k=-\infty}^{+\infty} f(t - kT_0) \tag{4}$$

in which

$$\varphi(t) = \frac{V_{IN}(t)}{V_\pi}\pi = \frac{V_{AC}}{V_\pi}\pi \cos(\omega_s t) = M\pi \cos(\omega_s t) \tag{5}$$

The input RF signal is set as a sinusoid wave to simplify the derivation. V_{AC} is the amplitude of the RF signal and V_π is the half-wave voltage of DO-MZM. M represents the modulation depth. ω_s is the angular frequency of the input RF signal. If we assume that a_k is a real number, after photo-detection the output voltage can be expressed as

$$V_1(t) = \frac{I + \Delta I(t)}{2}\Omega[1 + \sin\varphi(t)]\left[F_0 + 2\sum_{v=1}^{+\infty} F_v \cos(v\omega_0 t)\right] \tag{6}$$

$$V_2(t) = \frac{I + \Delta I(t)}{2}\Omega[1 - \sin\varphi(t)]\left[F_0 + 2\sum_{v=1}^{+\infty} F_v \cos(v\omega_0 t)\right] \tag{7}$$

in which

$$F_v = \sum_{u=-\infty}^{+\infty} a_u a_{u-v} \tag{8}$$

$$I + \Delta I(t) = RA^2(t) \tag{9}$$

Ω is the resistive load. R is the responsivity of the two photo-detectors (PD). I equals to R and $\triangle I(t)$ represents the noise current from the optical common-mode noise. F_v characterizes the power distribution of the OFC. Here we temporarily assume the bandwidth of PD is infinite in Eq. (6)-(7) and the actual frequency response of PD is later considered together with the post-detection electronics.

For the photonic sampled ADC, the analog bandwidth of the post-detection electronics is several times of the sampling rate in single path to avoid the intersymbol interference between pulses [12]. The spectral components in different Nyquist zones together with the temporal pulse shape are preserved, as shown in Fig. 2(a), and the detected signal can be calculated through $\varphi(t) = \sin^{-1}[(V_1(t) - V_2(t))/(V_1(t) + V_2(t))]$. However, photonic sampled ADC with Nyquist bandwidth larger than 10 GHz is rare as the requirement for the analog bandwidth of the electronic back-end becomes more stringent in the ultra-high speed system exceeding 20 GS/s when the number of parallel channels is limited [16], [17]. In comparison, the preprocessor for ADC based on photonic down-conversion shown in Fig. 2(b) requires an analog bandwidth equal to the Nyquist bandwidth, namely half of the sampling rate in the post-detection electronics. The loss of spectral components
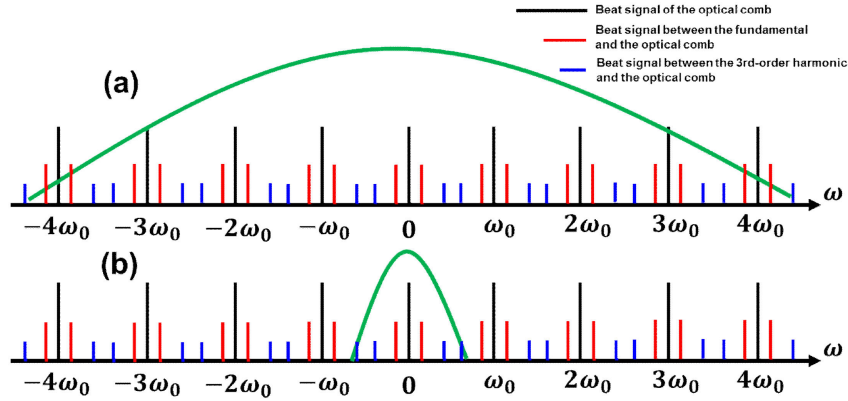
Fig. 2. Electrical spectrum after photo-detection by a PD with an infinite response bandwidth for (a) the photonic sampled ADC with an analog bandwidth several times of the repetition rate and (b) the photonic down-conversion preprocessor with an analog bandwidth half of the repetition rate. The green line represents the frequency response of low-pass filters.

except for those in the first Nyquist zone degenerates the carrier from pulse to DC and prevents the rematch of the fundamental signal and nonlinearity in different Nyquist zones of the baseband. The mismatch indicates the necessity of reconsidering the arcsine equalization in the proposed system.

The low-pass filter only preserves the spectral components in the first Nyquist zone $[-\omega_0/2, \omega_0/2]$, and with the Bessel function expansion as

$$\sin\varphi(t) = -2\sum_{m=1}^{+\infty}(-1)^m J_{2m-1}(M\pi)\cos[(2m-1)\omega_s t], \tag{10}$$

Eq. (6)-(7) can change to

$$V_1(t) = \frac{I+\Delta I(t)}{2}\Omega\left[F_0 - 2\sum_{m=1}^{+\infty}F_{n_m}(-1)^m J_{2m-1}(M\pi)\cos[(2m-1)\omega_s t - n_m\omega_0 t]\right] \tag{11}$$

$$V_2(t) = \frac{I+\Delta I(t)}{2}\Omega\left[F_0 + 2\sum_{m=1}^{+\infty}F_{n_m}(-1)^m J_{2m-1}(M\pi)\cos[(2m-1)\omega_s t - n_m\omega_0 t]\right] \tag{12}$$

in which $-\omega_0/2 < (2m-1)\omega_s - n_m\omega_0 < \omega_0/2$, and the integer n_m satisfying

$$n_m = floor\left[(2m-1)\frac{\omega_s}{\omega_0} + \frac{1}{2}\right] \tag{13}$$

where the symbol *floor* means the rounding down function.

2.2. Arcsine Equalization in the Photonic Down-Conversion System

The influence of F_v is temporarily neglected and will be discussed in Section 3. With this approximation Eq. (11)–(12) transform to

$$V_1(t) = \frac{V_0 + \Delta V_0(t)}{2}[1 + \sin(M\pi\cos\omega_r t) + NL(t)] \tag{14}$$

$$V_2(t) = \frac{V_0 + \Delta V_0(t)}{2}[1 - \sin(M\pi\cos\omega_r t) - NL(t)] \tag{15}$$

where $V_0(t) = F_0 I(t)\Omega$, $\Delta V_0(t) = F_0 \Delta I(t)\Omega$, and $\omega_r = \omega_s - n_1\omega_0$. $NL(t)$ is expressed as

$$NL(t) = 4\sum_{m=2}^{+\infty}(-1)^m J_{2m-1}(M\pi)\sin\frac{(2m-1)(\omega_m - \omega_r)t}{2}\sin\frac{(2m-1)(\omega_m + \omega_r)t}{2} \tag{16}$$

in which we define

$$\omega_m = \omega_s - \frac{n_m\omega_0}{2m-1}, \quad \text{where } m = 2, 3, 4\ldots \tag{17}$$

$NL(t)$ representing the residual nonlinearity that is introduced from the inequality of ω_m and ω_r. The value of $NL(t)$ depends on the input frequency and the harmonics we concentrate on. For instance, the third-order harmonic is often the dominant source of nonlinearity when the MZM is biased at the quadrature point. For simplicity we rule out the other higher-order harmonics in Eq. (16) and only preserve the item with $m = 2$ representing the third-order harmonic

$$NL(t) \approx 4J_3(M\pi)\sin\frac{3(\omega_2 - \omega_r)t}{2}\sin\frac{3(\omega_2 + \omega_r)t}{2} \tag{18}$$

The sinusoid transfer function of MZM can be removed completely by the arcsine equalization only when $NL(t)$ equals to zero, and there should be a relationship of $\omega_2 = \omega_r$, corresponding to

$$floor\left(\frac{3\omega_s}{\omega_0} + \frac{1}{2}\right) = 3floor\left(\frac{\omega_s}{\omega_0} + \frac{1}{2}\right) \tag{19}$$

The solution of Eq. (19) is

$$k\omega_0 - \omega_0/6 \le \omega_s \le k\omega_0 + \omega_0/6, \text{ where } k \in \mathbb{N}, \text{ and } \omega_s > 0 \tag{20}$$

$NL(t)$ equals to zero within the above periodic frequency range, and the output voltage after the arcsine equalization is

$$V_{out}(t) = \frac{V_\pi}{\pi}\sin^{-1}\left(\frac{V_1(t) - V_2(t)}{V_1(t) + V_2(t)}\right)$$

$$= MV_\pi\cos\left[(\omega_s - k\omega_0)t\right] \tag{21}$$

The result in Eq. (21) is a frequency down-converted signal at $\omega_r = \omega_s - k\omega_0$ where k equals to n_1 mathematically. Eq. (21) shows that both the modulation nonlinearity of the MZM and the common-mode noise $\Delta V_0(t)$ are eliminated when the signal frequency is within the periodic range $[k\omega_0 - \omega_0/6, k\omega_0 + \omega_0/6]$ while only the common-mode noise $\Delta V_0(t)$ is eliminated when the signal is outside the periodic frequency range. Besides, Eq. (21) proves that the arcsine equalization is more effective than the balanced detection for the photonic down-conversion preprocessor. The nonlinearity cannot be suppressed for any frequency and there will be residual common-mode noise $\Delta V_0(t)$ in the output of the balanced detection according to the subtraction result of Eq. (14) and Eq. (15).

The suppression of nonlinearity in the arcsine equalization can be explained by the following physical image. When the OFC is modulated by the RF signal, each frequency comb line will generate sidebands which are frequency-shifted from each comb line by ω_s, $3\omega_s$, $5\omega_s$.... There are no even-order sidebands as the MZM is biased at the quadrature point. Among all the beats between the sidebands and the frequency comb lines, both the beats at $|\omega_s - k\omega_0|$ and $|3\omega_s - 3k\omega_0|$ are within the first Nyquist zone $[-\omega_0/2, \omega_0/2]$ when the signal frequency ω_s is within $[k\omega_0 - \omega_0/6, k\omega_0 + \omega_0/6]$. Besides, the beats at $|\omega_s - k\omega_0|$ and $|3\omega_s - 3k\omega_0|$ are the first two items of the sine function expansion in Eq. (14)–(15) and composite a good approximation of $\sin[M\pi\cos(\omega_s - k\omega_0)t]$. When the signal frequency ω_s is outside the range $[k\omega_0 - \omega_0/6, k\omega_0 + \omega_0/6]$, the beat at $|3\omega_s - 3k\omega_0|$ generated by the third-order harmonic of the signal and the $3k^{th}$ frequency comb line is located outside the first Nyquist zone and thus filtered out by the low-pass filter. The sinusoid function cannot be recovered on that occasion. However, when M is small enough, the sine function of Eq. (14)–(15) can be well approximated only by the beat at $|\omega_s - k\omega_0|$, and the effective suppression of nonlinearity will not be limited by the periodic frequency range in Eq. (20).

If we introduce random noises including thermal noise and flicker noise from the electronic circuits and quantizing noise from the quantization process, Eq. (14)–(15) change to

$$V_1(t) = \frac{V_0 + \Delta V_0(t)}{2}[1 + \sin(M\pi \cos \omega_r t) + NL(t)] + d_1(t) \tag{22}$$

$$V_2(t) = \frac{V_0 + \Delta V_0(t)}{2}[1 - \sin(M\pi \cos \omega_r t) - NL(t)] + d_2(t) \tag{23}$$

where $d_1(t)$ and $d_2(t)$ represent statistically independent noises from electronic circuits and quantization process. After the arcsine equalization based on Eq. (22)–(23), the output is expressed as

$$V_{out}(t) = \frac{V_\pi}{\pi}\sin^{-1}\left(\frac{[V_0 + \Delta V_0(t)][\sin(M\pi \cos \omega_r t) + NL(t)] + d_1(t) - d_2(t)}{V_0 + \Delta V_0(t) + d_1(t) + d_2(t)}\right) \tag{24}$$

2.3. SINAD of the System

The calculation of SINAD can be decomposed of the calculation of SFDR and SNR, and we first calculate SFDR. The nonlinearity is well-suppressed within $[k\omega_0 - \omega_0/6, k\omega_0 + \omega_0/6]$, therefore the SFDR does not need to be taken into account within the frequency range. For the signal outside $[k\omega_0 - \omega_0/6, k\omega_0 + \omega_0/6]$, the non-zero $NL(t)$ in Eq. (24) induces nonlinearity. When the SFDR is higher than 40 dB to support an ENOB over 6, the modulation depth M should be smaller than 0.15. Considering the mathematical approximation as $\sin^{-1}(x) \approx x$ when x is small, for small $M < 0.15$, Eq. (24) can be approximated by

$$V_{out}(t) \approx \frac{V_\pi}{\pi}[\sin(M\pi \cos \omega_r t) + NL(t)] \approx \frac{2V_\pi}{\pi}\sum_{m=1}^{2}(-1)^m J_{2m-1}(M\pi)\cos[(2m-1)\omega_m t] \tag{25}$$

Therefore when M is small, the SFDR for the signal outside $[k\omega_0 - \omega_0/6, k\omega_0 + \omega_0/6]$ after the equalization is

$$SFDR \approx 10\log_{10}\frac{J_1^2(M\pi)}{J_3^2(M\pi)} \tag{26}$$

In addition to the analysis of nonlinearity, we also calculate the SNR after the equalization, and especially evaluate the influence of $d_1(t)$ and $d_2(t)$ in Eq. (24). We calculate the Taylor expansion of V_{out} in Eq. (24) around (0, 0) and only preserve the first-order items.

$$V_{out}(d_1(t), d_2(t)) = V_{out}(0, 0) + d_1\frac{\partial V_{out}}{\partial d_1}\bigg|_{d_1=d_2=0} + d_2\frac{\partial V_{out}}{\partial d_2}\bigg|_{d_1=d_2=0} + O(d_1(t), d_2(t)) \tag{27}$$

The variance of V_{out} can be calculated as

$$\sigma_{V_{out}}^2 = \left(\frac{\partial V_{out}}{\partial d_1}\bigg|_{d_1=d_2=0}\right)^2\sigma_{d_1}^2 + \left(\frac{\partial V_{out}}{\partial d_2}\bigg|_{d_1=d_2=0}\right)^2\sigma_{d_2}^2 \tag{28}$$

The random noises from electronics in the two channels are statistically independent and their variances are the same if we take flicker noise, thermal noise and quantizing noise into account

$$\sigma_{d_1}^2 = \sigma_{d_2}^2 = \sigma^2 \tag{29}$$

where σ is a constant and depends on the electronic ADC in use. Based on Eq. (28)-(29), the variance of the output voltage can be expressed as

$$\sigma_{V_{out}}^2 = \frac{V_\pi^2}{\pi^2 V_0^2}\left[\frac{1 - \sin(M\pi \cos \omega_r t) - NL(t)}{1 + \sin(M\pi \cos \omega_r t) + NL(t)} + \frac{1 + \sin(M\pi \cos \omega_r t) + NL(t)}{1 - \sin(M\pi \cos \omega_r t) - NL(t)}\right]\sigma^2 \tag{30}$$

which means that the output noise power of the whole system no longer remains as a constant. The SNR of the system for both frequency ranges equals to the ratio of the signal power to the

noise power, expressed as

$$SNR = 10\log_{10}\left(\frac{M^2 V_\pi^2}{2\sigma_{V_{out}}^2}\right) \tag{31}$$

The SINAD for the signal outside $[k\omega_0 - \omega_0/6, k\omega_0 + \omega_0/6]$ can be calculated based on Eq. (26) and Eq. (31). Particularly when M is small ($M < 0.15$), Eq. (30) can be approximated by

$$\sigma_{V_{out}}^2 \approx \frac{2V_\pi^2}{\pi^2 V_0^2}\sigma^2 \tag{32}$$

Eq. (32) approximate the output noise power of system in Eq. (30) as a constant when M is small for the convenience of calculation. Therefore the SINAD for the signal outside $[k\omega_0 - \omega_0/6, k\omega_0 + \omega_0/6]$ when M is small ($M < 0.15$) can be expressed as

$$\text{SINAD}_1 = -10\log_{10}\left(10^{-\frac{SNR}{10}} + 10^{-\frac{SFDR}{10}}\right) \approx -10\log_{10}\left(\frac{J_3^2(M\pi)}{J_1^2(M\pi)} + \frac{4\sigma^2}{\pi^2 M^2 V_0^2}\right) \tag{33}$$

The optimal modulation depth M can be obtained by calculating the derivative of the function in the bracket of Eq. (33).

Since the nonlinearity is well-suppressed for the signal frequency within $[k\omega_0 - \omega_0/6, k\omega_0+\omega_0/6]$ via the arcsine equalization, the corresponding SINAD equals to the SNR and is expressed as

$$\text{SINAD}_2 = SNR = 10\log_{10}\left(\frac{M^2 V_\pi^2}{2\sigma_{V_{out}}^2}\right) \tag{34}$$

There is also an optimal M for SINAD_2 and the optimal M must be larger due to the effective suppression of nonlinearity. Therefore, the approximation in Eq. (32) cannot be applied here for the signal frequency within $[k\omega_0 - \omega_0/6, k\omega_0 + \omega_0/6]$. The output noise power of the whole system in Eq. (34) should be calculated through the integral as following

$$\sigma_{V_{out}}^2 = \frac{V_\pi^2 \sigma^2 \omega_r}{6\pi^3 V_0^2} \int_0^{\frac{6\pi}{\omega_r}} \left[\frac{1 - \sin(M\pi\cos\omega_r t) - NL(t)}{1 + \sin(M\pi\cos\omega_r t) + NL(t)} + \frac{1 + \sin(M\pi\cos\omega_r t) + NL(t)}{1 - \sin(M\pi\cos\omega_r t) - NL(t)}\right]dt \tag{35}$$

SINAD_1 in Eq. (33) and SINAD_2 in Eq. (34) are both uncorrelated with the signal frequency within respective frequency range. We numerically evaluate the relationship between the signal frequency and the SINAD after the equalization, as shown in Fig. 3. The simulation results in blue lines are based on Eq. (22)–(23) without any mathematical approximation and thus more accurate. The approximation results in red lines are based on Eq. (33)–(34) with proper mathematical approximations. The variance of $d_1(t)$ and $d_2(t)$ is $5.0 \times 10^{-6} V_0^2$, and the variance of $\triangle V_0$ is $9.4 \times 10^{-6} V_0^2$. The influence of F_v is also included in the simulation results.

There is no big difference (<1 dB) of SINAD for both frequency ranges with small M (<0.15), indicating that small modulation depth is suitable for the detection of a broadband signal with unknown carrier frequency and bandwidth. The SINAD difference becomes significant when M is larger than 0.25, and the SINAD within $[k\omega_0 - \omega_0/6, k\omega_0 + \omega_0/6]$ is improved a lot around $M = 0.25$ with the same simulation parameters of the optical power and noise power. It means that we can simultaneously use a high repetition-rate OFC and medium modulation depth like 0.25 to digitize a broadband signal with known carrier frequency and bandwidth more precisely given the same optical power.

Comparing the red lines with the blue lines, it is also shown in Fig. 3 that SINAD_2 in Eq. (34) works as a good approximation within $[k\omega_0 - \omega_0/6, k\omega_0 + \omega_0/6]$ for any M while SINAD_1 in Eq. (33) works as a good approximation outside $[k\omega_0 - \omega_0/6, k\omega_0 + \omega_0/6]$ for small and moderately large M. For large M like 0.45, Eq. (26) and Eq. (32) cannot be established and SINAD_1 cannot be used as an approximation outside $[k\omega_0 - \omega_0/6, k\omega_0 + \omega_0/6]$.

Besides, when the modulation depth M is fixed, the SINAD_2 within $[k\omega_0 - \omega_0/6, k\omega_0 + \omega_0/6]$ slowly decreases while the SINAD_1 outside $[k\omega_0 - \omega_0/6, k\omega_0 + \omega_0/6]$ slowly increases with the
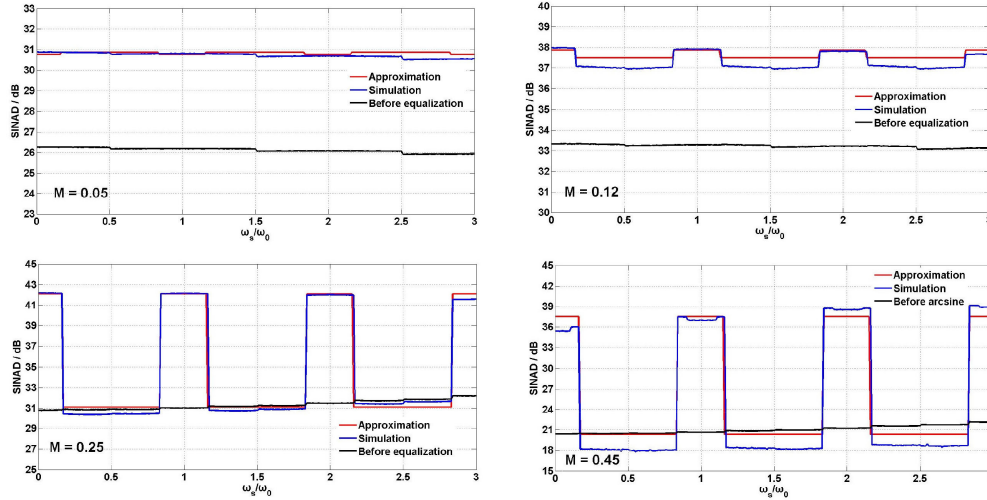
Fig. 3. The relationship between signal frequency and SINAD before and after the equalization. The blue lines are based on simulation results from Eq. (22)–(23) with no approximation and the red lines are based on the estimation results from Eq. (33)–(34). The black lines demonstrate simulation results of the SINAD before the arcsine equalization.

frequency because of different F_v for the fundamental signal and third-order harmonic. For large M like 0.45, on the contrary, F_v reverses the trend of the SINAD within $[k\omega_0 - \omega_0/6,\ k\omega_0 + \omega_0/6]$ through the fifth-order harmonic, which is reduced from the decrease of F_v. For $M > 0.5$, the arcsine function becomes a multi-value function and the equalization becomes invalid.

2.4. Relationship With the Electronic ADC

Up to this point, we assume the full scale of the back-end electronic ADC is infinite. In a practical system, the amplitude V_Q of the alternating voltage in either Eq. (22) or Eq. (23) to be quantized should not exceed the measurement range $[-V_{Full}, +V_{Full}]$ of the quantizer in the electronic ADC system. The amplitude V_Q before quantization in either channel is expressed as

$$V_Q = V_0 J_1(M\pi) \leq V_{Full} \tag{36}$$

With Eq. (36), we can transform Eq. (34) to

$$\text{SINAD}_2 = 10\log_{10}\left(\frac{M^2 V_\pi^2}{2\sigma_{V_{out}}^2}\right) \leq 10\log_{10}\left(\frac{V_{Full}^2}{2\sigma^2}\right) + G = \text{SNR}_Q + G \tag{37}$$

SNR_Q evaluates the sampling precision of the electronic ADC in use and supporting circuits like pre-amplifiers as a whole. The random noise rather than the nonlinearity is usually the bottleneck of sampling precision in the electronic ADC system when the electrical amplifier is not saturated. Therefore, the SINAD_Q is approximately equal to SNR_Q and the ENOB of the electronic ADC system can be calculated from $\text{ENOB}_Q = (\text{SNR}_Q - 1.76)/6.02$. The flicker noise and thermal noise of the supporting circuits and the quantizing noise from quantization are all included when calculating SNR_Q to obtain a practical ENOB_Q. G represents the maximum gain of SINAD from the photonic preprocessor with the arcsine equalization compared to SNR_Q of the electronic ADC, expressed as

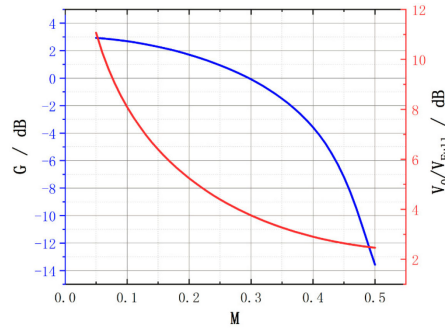$$G = 10\log_{10}\left(\frac{M^2 V_\pi^2 \sigma^2}{J_1^2(M\pi) V_0^2 \sigma_{V_{out}}^2}\right) \tag{38}$$

Fig. 4. The blue curve (left axis) represents the relationship between M and the maximum gain of the proposed photonic down-conversion system. The red curve (right axis) characterizes the relationship between M and requirement of the optical power in order to satisfy $V_Q = V_{Full}$.

The actual gain of the photonic preprocessor equals to G only when the amplitude V_Q before quantization equals to the full scale V_{Full} of the quantizer. The relationship between G and the modulation depth M is calculated based on Eq. (35) and Eq. (38) given that the full scale of the quantizer is unchanged, as shown in the blue curve of Fig. 4.

The maximum gain is 3 dB at a small M, and on that occasion $SINAD_2$ is given by

$$SINAD_2 \approx SNR_Q + 3 \; dB \tag{39}$$

Eq. (39) indicates that the ENOB of the proposed system can maximally be 0.5 better than that of the electronic ADC in use. Fig. 4 shows that the G gradually decreases with the increase of M, and becomes negative around $M = 0.3$. As discussed above, the amplitude V_Q before quantization needs to be equal to the full range V_{Full} of the quantizer so as to make the actual gain of SINAD equal to G. Therefore, the smaller M we choose, the higher the optical power needs to be, as shown in the red curve of Fig. 4. For example, the power of the OFC for $M = 0.05$ should be 5.8 dB higher than that for $M = 0.2$ in order to reach the gain upper-limit of SINAD. In practice, there is a trade-off between the optical power and the optimal M. The optimal M should be chosen as the smaller value between the optimal M calculated from Eq. (34) and the M that generates the output voltage V_Q which is equal to V_{Full} of the quantizer. Proper configuration of the modulation depth M can shift some of the burden from constantly increasing the optical power of the OFC and make the setup more feasible. Besides, despite that the above derivation is based on Eq. (34), these conclusions can be extended to the SNR of signals outside $[k\omega_0 - \omega_0/6, k\omega_0 + \omega_0/6]$ as long as the gain of SNR is not covered by the residual nonlinearity after the equalization.

To sum up, we derive the working principle and evaluate the performance of the photonic down-conversion preprocessor for ADC with arcsine in this section. The optical common-mode noise can be eliminated for any frequency through the method and the nonlinearity can be well suppressed within $[k\omega_0 - \omega_0/6, k\omega_0 + \omega_0/6]$. For applications such as communication and measurement where the bandwidth and carrier frequency of the signal is known in advance, we can tune or multiply the repetition rate of pulses so as to make the signal match the frequency range and be digitized with high precision and low optical power. However, when the bandwidth and carrier frequency of the signal is totally unknown like reconnaissance, small modulation depth and high optical power should be used instead to overcome the nonlinearity and guarantee the same precision as the former scenario. The ENOB of the proposed system for both scenarios can maximally be 0.5 larger than that of the electronic ADC.

3. Numerical and Experimental Results

We first evaluate the change of F_v with different v values and different OFCs, as shown in Fig. 5. The red, blue and green lines are calculated based on the OFCs with uniform amplitude,
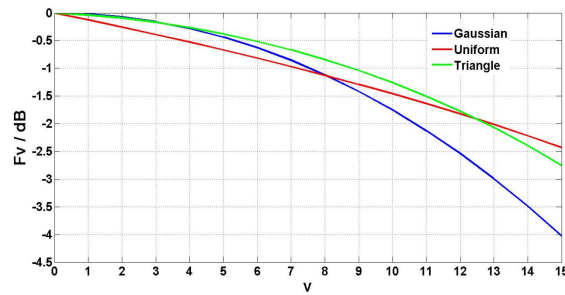
Fig. 5. The relationship between F_v and v for three different OFCs: the red, blue and green line is based on a comb with 35 spectral lines of uniform amplitude, Gaussian-shape amplitude and triangle-shape amplitude respectively.
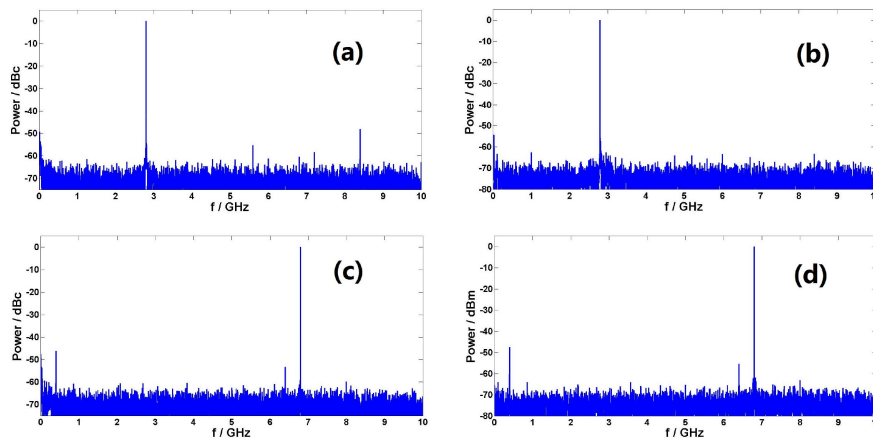

Fig. 6. The FFT results of the digitized signal at 42.8 GHz before (a) and after (b) the arcsine equalization, 46.8 GHz before (c) and after (d) the arcsine equalization.

Gaussian-shape amplitude and triangle-shape amplitude respectively. There are 35 spectral lines for each OFC. Considering that the third-order harmonic is often the dominant nonlinearity, it can be calculated from Eq. (13) that v is smaller than 7 for the Q-band signal and OFC of higher than 20 GHz. It means that F_v changes less than 1 dB with v for all three OFCs, validating the assumption in section 2.

We also verify the effect of the arcsine equalization on two types of frequency ranges. Signals at 42.8 GHz and 46.8 GHz are experimentally digitized through the proposed system with an OFC of 20 GHz. The experimental setup is shown in Fig. 1, and the OFC is generated through optical frequency comb generator (OFCG) after a narrow-linewidth seed laser (Teraxion, PS-NLL-1550.12-080-200-A1). Single stage erbium-doped fiber amplifier (EDFA, Amonics AEDFA-PM-DWDM-23-B-FC) is used to compensate for the optical loss from the OFCG while maintaining low intensity and phase noise [18]–[20]. The theoretical shape of the optical spectrum is triangle and we tune the driving frequency slightly to generate a 4.5-nm trapezoid optical spectrum to eliminate the initial non-zero spectral phase as much as possible [21], [22]. The PD (U2t V2150R) converts the optical signal from DO-MZM (Eospace AX-1x2-0MVS-40) to electrical signal and send it to the electronic ADC. The two electronic ADCs in the setup are the two channels of a high-speed oscilloscope (Kesight DSOZ634A). The equivalent ENOB of each channel is 5.7 respectively. Fig. 6(a) and (b) show the spectra of digitized 42.8 GHz signal before and after the equalization. Fig. 6(c) and (d) show the spectra of digitized 46.8 GHz signal before and after the equalization.
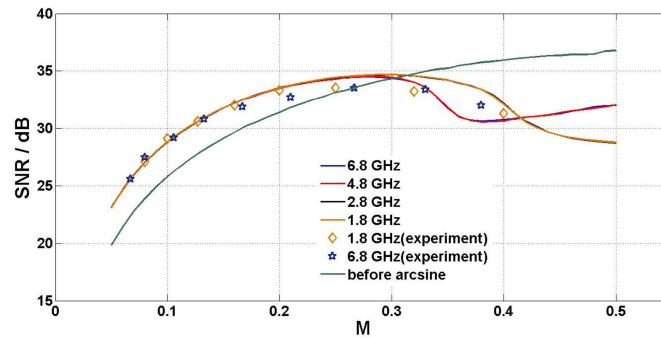
Fig. 7. Numerical and experimental SNR results of baseband signals at different frequencies with different modulation depth. The lines represent the simulation results and dots represent the experimental results. The red line overlaps with the blue line and the deep yellow line overlaps with the black line.

Due to the periodicity of the OFC, the fundamental tones of the digitized 42.8 GHz and 46.8 GHz signals are down-converted and aliased at 2.8 GHz and 6.8 GHz respectively, while the third-order harmonics are aliased at 8.4 GHz and 0.4 GHz respectively. For 42.8 GHz signal located within [36.7 GHz, 43.3 GHz], the third-order harmonic is reduced by 16.3 dB while the third-order harmonic of 46.8 GHz signal is reduced only by 1.2 dB. The weak suppression of third-order nonlinearity for signals located outside [36.7 GHz, 43.3 GHz] verifies our discussions in section 2. The SNR is improved more than 3 dB as expected for both signals when the modulation depth $M =$ 0.12. However, the improvement of SNR may not always be the case as the aggregate noise power of the system is correlated with the signal and nonlinearity at the same time, as shown in Eq. (30).

The half-wave voltage of our MZM is quite large above 40 GHz (16.7V@43 GHz) and relatively small below 10 GHz (4.5V@2GHz, 5.3V@6 GHz). It is easier to realize large modulation depth below 10 GHz. Therefore, we digitize signals at 1.8 GHz and 2.8 GHz located within [0 GHz, 3.3 GHz], and signals at 4.8 GHz and 6.8 GHz located outside [0 GHz, 3.3 GHz] to test the relationship between SNR and modulation depth. As a proof of concept, the optical power is configured so as to make the voltage amplitude V_Q before quantization match the full scale of the quantizer when $M = 0.4$ so that the relationship between the SNR and modulation depth can be fully observed without being affected by the measurement range of the quantizer. The numerical and experimental results are shown in Fig. 7. The numerical simulation is based on Eq. (22)–(23) with no mathematical approximation, and the values of parameters in the simulation are determined by matching the results of the first experiment point and the simulation with the same M.

Although the random noises $d_1(t)$ and $d_2(t)$ in electronic ADCs are uncorrelated with M, the output noise of the whole arcsine system is a nonlinear mathematical function of $d_1(t)$, $d_2(t)$, M shown in Eq. (35) and is correlated with M, especially for a medium or large M. The arcsine function cannot be approximated as a linear function for a medium or large M because $sin^{-1}(x) \approx x$ is not established with large x. Therefore, the aggregate noise power first increases very slowly (almost unchanged) with M (equal to Eq. (32)) but then rapidly after the linear approximation of arcsine becomes invalid. The signal power first increases rapidly with M but then slowly in the form of Bessel function. The SNR should first increase but then decrease according to the above analysis, which is verified by the numerical and experimental results in Fig. 7.

The curves in Fig. 7 are not identical for different frequencies depending on whether the frequency is within [0 GHz, 3.3 GHz] or not, because a non-zero $NL(t)$ affects the SNR in Eq. (31). Moreover, the theoretical results show that the arcsine equalization provides an over 3-dB improvement of SNR for small M (<0.15), while the improvement decreases with the increase of M and disappears after M = 0.3. The measured SNR is a little lower (<1 dB) than the theoretical calculation, resulting from the unbalanced path after the two outputs of the MZM. Particularly the experimental result of the 6.8 GHz signal at $M = 0.38$ is better than the theoretical prediction. It
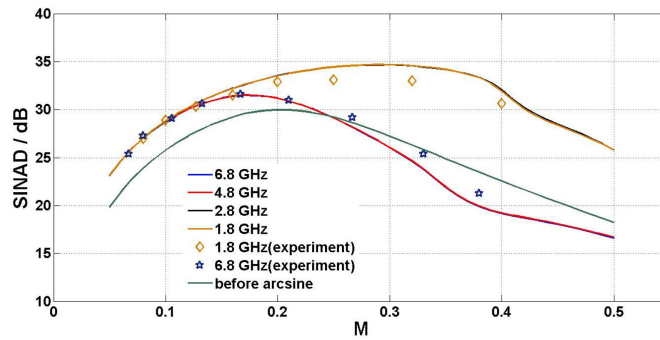
Fig. 8. Numerical and experimental SINAD results of baseband signals at different frequencies with different modulation depth. The lines represent the simulation results and dots represent the experimental results. The red line overlaps with the blue line and the deep yellow line overlaps with the black line.
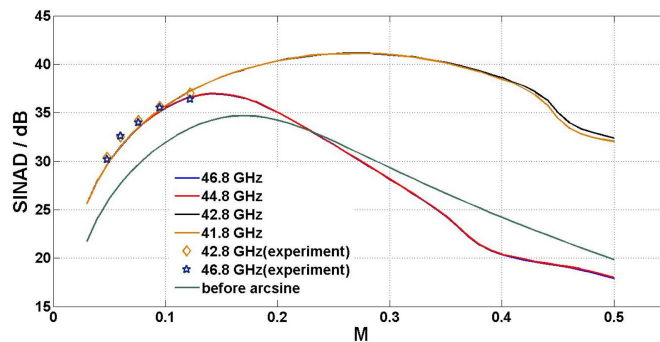

Fig. 9. Numerical and experimental SINAD results of millimeter-wave signals at different frequencies with different modulation depth. The lines represent the simulation results and dots represent the experimental results. The red line overlaps with the blue line and the deep yellow line partially overlaps with the black line.

is probably the result of residue non-zero phase of our OFC [20]–[22], reducing the third-order nonlinearity and NL(t) of the 6.8 GHz signal.

The corresponding SINAD is also calculated and measured, as shown in Fig. 8. For 1.8 GHz and 2.8 GHz signals located within [0 GHz, 3.3 GHz], the shape of the SINAD curve is similar to that of the SNR curve, only slightly downward when M is large. The similarity is attributed to the suppression of nonlinearity with arcsine when M is smaller than 0.45, making random noise the dominant source of distortion. Larger M can induce significant higher-order harmonics that fail to satisfy $\omega_m = \omega_r$ for $m>2$. However, even for M exceeding 0.2, the SINAD of 4.8 GHz and 6.8 GHz signals outside the frequency range is obviously worse than the SNR. The experiment results verify the above theoretical predictions, and the small difference is due to the unbalanced path and imperfect comb phase as discussed before.

Despite the high half-wave voltage of our MZM above 40 GHz, signals at higher than 40 GHz can still be digitized with limited modulation depth, as shown in Fig. 9. We use the quantizer with a smaller equivalent measuring range (from 80 mV to 40 mV) and also smaller noise power than that used in the baseband sampling. The optical power is increased from the output of EDFA by 2.8 dB. The amplitude V_Q before quantization matches the full range of the new quantizer when $M =$ 0.12. The shape of curves is similar to that of the baseband detection in Fig. 9 and the discussions before can still apply here. It should be emphasized that although the optimized working point (M = 0.15 for broadband signals at 40~50 GHz and M = 0.27 for signals at 36.7~43.4 GHz) is not
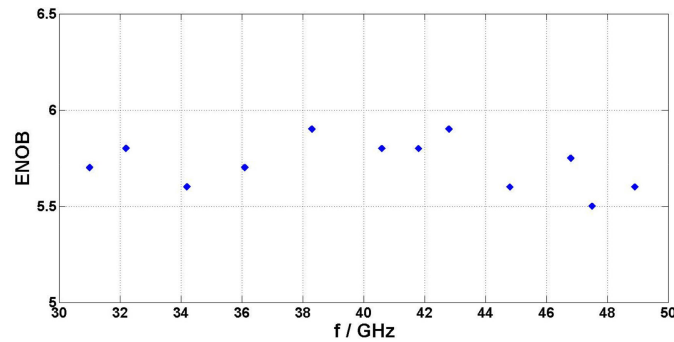
Fig. 10. The relationship between ENOB and signal frequency. The ENOB of the proposed system is 5.8∼5.9 within the frequency range while the ENOB outside the frequency range is 0.1∼0.3 lower.

realized due to our MZM, we find the best configuration ($M = 0.12$) within our reach thanks to the analysis in Section 2.

We also measure the relationship between ENOB of the proposed system and the signal frequency with fixed modulation depth of 0.12, as shown in Fig. 10. The bandwidth of the proposed system is 10 GHz and single-tone signals from 31 GHz to 48.9 GHz are tested. The ENOB of our electronic ADC is 5.7. The calculated ENOB of the proposed system is from 5.8 to 5.9 within [36.7 GHz, 43.3 GHz] while the ENOB is 0.1 to 0.3 lower outside this frequency range. Compared with the configuration in Fig. 8, the configuration in Fig. 9–10 is more suitable for applications like reconnaissance where the carrier frequency and bandwidth of the signal is totally unknown. The difference of precision is not significant for different frequencies. The overall lower ENOB for frequency higher than 44 GHz is probably due to the frequency response of EO and OE conversion and can be further compensated with calibration and digital filtering.

4. Discussion on FOM

There have been some well-known discussions on the figure of merit (FOM) of Nyquist sampling systems or bandpass sampling systems [23], [24], which help to characterize the performance of the whole system from perspectives of carrier frequency, bandwidth and precision. However, the timing jitter and phase noise in the previous definitions are treated as exogenous variables which are not correlated with the repetition rate of the clock. In fact, the timing jitter and phase noise of electrical or optical clock theoretically increase with the sampling rate if there is no improvement of the structure. Moreover, the previous definitions are not flexible enough as our concentration on amplitude noise and phase noise are not always equal for different types of signals. If the bandwidth of a millimeter-wave signal to be digitized is only 100 MHz, the amplitude noise does not need to be taken into account, as the precision of digitizing is mainly limited by the large carrier frequency and phase noise on that occasion. The amplitude noise becomes the main limitation of the precision and has to be evaluated when the bandwidth of the signal is up to 10 GHz. Here we would like to propose a new FOM that, as we believe, can be used to evaluate bandpass sampling systems more comprehensively and flexibly.

The SNR of the bandpass sampling system determined by the amplitude noise can be characterized as a function of bandwidth given the same performance of electrical amplifiers and quantizers. The relationship can be expressed as

$$SNR_A \propto f_{BW}^{-1} \tag{40}$$

where f_{BW} represents the bandwidth of the proposed system.

The SNR of the bandpass sampling system determined by the phase noise is affected by the product of timing jitter and signal frequency [8]. For bandpass sampling systems with photonic
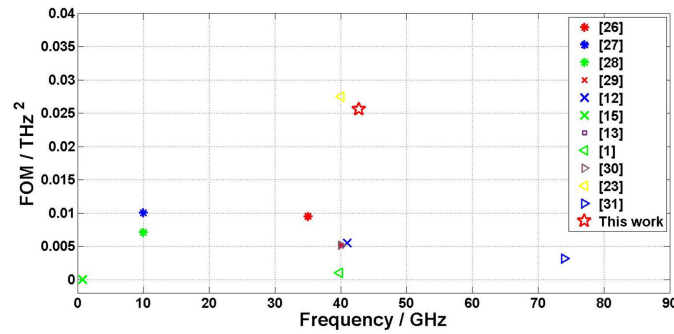
Fig. 11. The relationship between the FOM with $\alpha = \beta = 1$ and frequency among bandpass sampling systems.

technologies, the SNR of the system determined by the phase noise is affected by the product of timing jitter of the OFC and input signal frequency applied on the MZM. The signal frequency can be approximated by the carrier frequency f_c for a bandpass signal. The timing jitter calculated from the phase noise in the frequency domain is more complicated and usually not independent of the repetition rate. It has been shown that the single sideband (SSB) phase noise increases by 6 dB with frequency doubling [25]. The doubling of the repetition rate also mathematically doubles the Nyquist bandwidth, which is the integral interval of the phase noise to calculate the timing jitter. Overall timing jitter doubles theoretically when the repetition rate increases by three times, which means

$$t_j \propto \sqrt{f_s} \propto \sqrt{f_{BW}} \tag{41}$$

where t_j is the timing jitter and f_{BW} equals to half of the sampling rate f_s according to the Nyquist theorem. The SNR of the system determined by the phase noise is

$$SNR_T \propto t_j^{-2} f_c^{-2} \propto f_{BW}^{-1} f_c^{-2} \tag{42}$$

It should be emphasized that the relationship in Eq. (42) is established for both the photonic sampled system and photonic down-conversion system when the input signal is a bandpass signal. This can be proved through the analysis of the phase noise or from a simpler perspective of the electrical spectrum of digitized signals. As the power of the phase noise from the OFC and power of the signal are proportionally reduced by the low-pass filter in the frequency domain, the SNR_T of the down-conversion system remains unchanged after low-pass filtering. Therefore, the above analysis of the SNR_T in a temporal method is also applicable to the photonic down-conversion system.

Taking into account both the amplitude noise and the phase noise, the FOM can be defined as

$$FOM = 2^N f_{BW}^{\alpha/2} (f_c^2 f_{BW})^{\beta/2} = 2^N f_c^\beta f_{BW}^{(\alpha+\beta)/2} \tag{43}$$

where N equals to the ENOB, characterizing the precision of the system. α and β ($0 < \alpha, \beta \leq 1$) are the significance weights of the amplitude noise and phase noise respectively.

Compared with previous definitions of the FOM, the newly-defined FOM treats the timing jitter as an endogenous variable, which we believe is more reasonable for the evaluation of the system. The clock with a higher sampling rate but the same timing jitter should be regarded as a better clock in our definition. Besides, the weights of the amplitude noise and phase noise as α and β provide us with flexibility of designing a customized FOM based on our specific demand. The α should be increased when the bandwidth of the signal to be digitized is large while the β should be increased when the carrier frequency is large.

In this work we specifically concentrate on broadband millimeter-wave signals, therefore both the amplitude noise and phase noise should be equally considered and we have $\alpha = \beta = 1$. Fig. 11 shows the FOMs of bandpass sampling systems including photonic sampled ADCs, time-stretched

ADCs and ADCs with the photonic down-conversion preprocessor when $\alpha = \beta = 1$. Thanks to the analysis of the optimal configuration in this work, the proposed system with the arcsine equalization using two quantizers with ENOB of 5.7 realizes an FOM close to the previous record.

5. Conclusions

In summary, for the first time we have comprehensively derived the working principle of a photonic down-conversion preprocessor for ADC with the arcsine equalization and exploited the different features of the equalization in the proposed system to optimize the performance. The evolution of the SNR and SINAD after the equalization is particularly analyzed. The numerical and experimental results show that both the SNR and the SINAD first increase but then decrease with the modulation depth. The common-mode noise is canceled and additional gain up to 3 dB of SNR is achieved for any frequency. The nonlinearity from large modulation depth is effectively suppressed within a periodic frequency range $[k\omega_0 - \omega_0/6, k\omega_0 + \omega_0/6]$. There is a trade-off between the system performance and the optical power of the OFC. Proper configuration of the modulation depth M helps to relief the burden of increasing the optical power of OFC. The model in this work provides us with guidance on the best configuration to exploit the potential of the system under different scenarios. As a proof of concept, millimeter-wave signals ranging from 31 GHz to 48.9 GHz are digitized through the proposed system with a bandwidth of 10 GHz, and the ENOB is 5.9 (@42.8 GHz) when the ENOB of the electronic ADC in use is 5.7. A new FOM is also defined to more comprehensively and flexibly evaluate bandpass sampling systems. Thanks to the analysis of optimization in this work, our system possesses a favorable performance compared with the previous record. With the optimal configuration of the proposed scheme, the ENOB of our system is now limited basically by the precision of electronic ADC and can be further improved through the update of electronic ADC.

References

[1] P. Ghelfi *et al.*, "A fully photonics-based coherent radar system," *Nature*, vol. 507, no. 7492, pp. 341–345, Mar. 2014.
[2] V. Ferragina *et al.*, "A 12.4 ENOB incremental A/D converter for high-linearity sensors read-out applications," in *Proc. IEEE Int. Symp. Circuits Syst.*, New Orleans, LA, USA, 2007, pp. 3582–3585.
[3] B. Mao *et al.*, "Impacts of ENOB on the performance of 112Gbps PDM-QPSK digital coherent receiver," in *Proc. Eur. Conf. Expo. on Opt. Commun.*, Geneva, Switzerland, 2011, pp. 1–3.
[4] X. Yang *et al.*, "Optical frequency comb based multi-band microwave frequency conversion for satellite applications," *Opt. Express*, vol. 22, no. 1, pp. 869–877, Jan. 2014.
[5] X. Fang *et al.*, "Ultra-broadband microwave frequency down-conversion based on optical frequency comb," *Opt. Express*, vol. 23, no. 13, pp. 17111–17119, Jan. 2015.
[6] X. Xie *et al.*, "Broadband photonic RF channelization based on coherent optical frequency combs and I/Q demodulators," *IEEE Photon. J.*, vol. 4, no. 4, Jul. 2012.
[7] T. Zhang *et al.*, "High-spectral-efficiency photonic frequency down-conversion using optical frequency comb and SSB modulation," *IEEE Photon. J.*, vol. 5, no. 2, Feb. 2013, Art. no. 7200307.
[8] F. Maloberti, *Data Converters*, Berlin, Germany: Springer Science & Business Media, 2007.
[9] C. Cox, E. Ackerman, and G. Betts, "The role of photonic and electronic gain in the design of analog optical links," in *Proc. IEEE Conf. Avionics Fiber-Opt. Photon.*, Minneapolis, MN, USA, 2005, pp. 1–2.
[10] G. Valley, "Photonic analog-to-digital converters," *Opt. Express.*, vol. 15, no. 5, pp. 1955–1982, Mar. 2007.
[11] J. Kim *et al.*, "Photonic subsampling analog-to-digital conversion of microwave signals at 40-GHz with higher than 7-ENOB resolution," *Opt. Express*, vol. 16, no. 21, pp. 16509–16515, Oct. 2008.
[12] A. Khilo *et al.*, "Photonic ADC: Overcoming the bottleneck of electronic jitter," *Opt. Exp.*, vol. 20, no. 4, pp. 4454–4469, Feb. 2012.
[13] A. Nejadmalayeri *et al.*, "A 16-fs aperture-jitter photonic ADC: 7.0 ENOB at 40 GHz," in *Proc. CLEO: Sci. Innovations*, Baltimore, MD, USA, 2011, pp. 1–2.
[14] P. Juodawlkis *et al.*, "Optically sampled analog-to-digital converters," *IEEE Trans. Microw. Theory Techn.*, vol. 49, no. 10, pp. 1840–1853, Oct. 2001.
[15] R. Williamson *et al.*, "Precision calibation of an optically sampled analog-to-digital converter," in *Proc. Dig. LEOS Summer Topical Meeting*, Vancouver, BC, Canada, 2003, pp. 22–23.
[16] M. Frankel *et al.*, "High-performance photonic analogue-digital converter," *Electron. Lett.*, vol. 33, no. 25, pp. 2096–2097, Dec. 1997.
[17] P. Juodawlkis *et al.*, "Optical down-sampling of wide-band microwave signals," *J. Lightw. Technol.*, vol. 21, no. 12, pp. 3116–3124, Dec. 2003.

[18] X. Xie *et al.*, "Low-noise and broadband optical frequency comb generation based on an optoelectronic oscillator," *Opt. Lett.*, vol. 39, no. 4, pp. 785–788, Feb. 2014.

[19] R. Guo *et al.*, "Photonic sub-sampling of signal at 43.1-GHz using optical comb based on an optoelectronic oscillator," in *Proc. IEEE Int. Topical Meeting Microw. Photon.*, Beijing, China, 2017, pp. 1–3.

[20] R. Guo *et al.*, "Programmable optical pulse repetition rate multiplication via spectral phase manipulation," *Opt. Express*, vol. 28, no. 3, pp. 4178–4193, Feb. 2020.

[21] S. Xiao *et al.*, "Toward a low-jitter 10 GHz pulsed source with an optical frequency comb generator," *Opt. Express*, vol. 16, no. 12, pp. 8498–8508, Jun. 2008.

[22] S. Xiao, L. Hollberg, and S. Diddams, "Generation of a 20 GHz train of sub-picosecond pulses with a stabilized optical frequency comb generator," *Opt. Lett.*, vol. 34, no. 1, pp. 85–87, Jan. 2009.

[23] D. Esman *et al.*, "Highly linear broadband photonic-assisted Q-band ADC," *J. Lightw. Technol.*, vol. 33, no. 11, pp. 2256–2262, Jun. 2015.

[24] R. Walden, "Analog-to-digital converter survey and analysis," *IEEE J. Sel. Areas Commun.*, vol. 17, no. 4, pp. 539–550, Apr. 1999.

[25] Y. Xu *et al.*, "Injection-locked millimeter wave frequency divider utilizing optoelectronic oscillator based optical frequency comb," *IEEE Photon. J.*, vol. 11, no. 3, Jun. 2019, Art. no. 5501508.

[26] J. Chou *et al.*, "Photonic bandwidth compression front end for digital oscilloscopes," *J. Lightw. Technol.*, vol. 27, no. 22, pp. 5073–5077, Nov. 2009.

[27] S. Gupta and B. Jalali, "Time-warp correction and calibration in photonic time-stretch analog-to-digital converter," *Opt. Lett.*, vol. 33, no. 22, pp. 2674–2676, Nov. 2008.

[28] G. Sefler *et al.*, "Distortion correction in a high-resolution time-stretch ADC scalable to continuous time," *J. Light. Technol.*, vol. 28, no. 10, pp. 1468–1476, May 2010.

[29] A. Wiberg *et al.*, "Demonstration of 40 GHz analog-to-digital conversion using copy-and-sample-all parametric processing," in *Proc. Opt. Fiber Commun. Conf.*, Los Angeles, CA, USA, 2012, pp. 1–3.

[30] A. Wiberg *et al.*, "Photonic preprocessor for analog-to-digital-converter using a cavity-less pulse source," *Opt. Express*, vol. 20, no. 26, pp. B419–B427, Dec. 2012.

[31] A. Wiberg *et al.*, "Demonstration of 74 GHz parametric optical sampled analog-to-digital conversion," in *Proc. Eur. Conf. Exhib. Opt. Commun.*, London, UK, 2013, pp. 1–3.